Cite this: *J. Mater. Chem. A*, 2017, 5, 7523

## Modified chalcogens with a tuned nano-architecture for high energy density and long life hybrid super capacitors†

Salah Abureden, Fathy M. Hassan, Gregory Lui, Serubbabel Sy, Rasim Batmaz, Wook Ahn, Aiping Yu and Zhongwei Chen\*

A novel *in situ* vanadium-modified NiCo<sub>2</sub>S<sub>4</sub> wrapped with graphene sheets was synthesized using a simple solvothermal technique. The vanadium-modified sample (VNCS) demonstrated superior electrochemical performance over graphene-wrapped NiCo<sub>2</sub>S<sub>4</sub> (GNCS) and pure NiCo<sub>2</sub>S<sub>4</sub> (NCS) samples, with a specific capacitance of 1340 F g<sup>-1</sup> at a current density of 2 A g<sup>-1</sup>. The VNCS sample also showed outstanding capacitance retention at 50 A g<sup>-1</sup> (1024 F g<sup>-1</sup>), which is 430% higher than that of the NCS sample. The cycling stability of VNCS was significantly improved by more than 140% compared to the NCS sample with less than 10<sup>-3</sup> F per cycle loss in capacitance after 10 000 cycles. We also report the fabrication of hybrid supercapacitors (HSCs) using three different materials for the faradaic electrode. The VNCS-HSCs showed significant improvements in all electrochemical performance measurements compared to NCS-HSCs. The capacitance retention at 50 A g<sup>-1</sup> was improved by more than 260% and the long cycling stability was improved by more than 180% after 10 000 cycles. The VNCS-HSC delivered an energy density of 45.9 W h kg<sup>-1</sup> at 0.87 kW kg<sup>-1</sup> and maintained a superior energy density of 33.6 W h kg<sup>-1</sup> at 9 kW kg<sup>-1</sup> indicating the excellent potential of this material in hybrid super capacitor applications.

Received 26th January 2017  
Accepted 2nd March 2017

DOI: 10.1039/c7ta00897j

rsc.li/materials-a

## Introduction

The development of reliable and effective energy storage solutions is of paramount importance in today's renewable energy landscape.<sup>1</sup> Specifically, devices with high energy and power densities that can retain high capacities over many cycles are sought after in order to provide stable energy storage for consumer and grid-scale applications.<sup>2-4</sup> Supercapacitors are a class of devices that are able to provide relatively good energy densities at high power densities over the course of many cycles.<sup>5-7</sup> However, one of the main shortcomings of supercapacitors is their low energy densities relative to current lithium ion battery technology. Therefore, the majority of recent research has been dedicated to fabricating supercapacitors with enhanced energy densities while still operating at higher power densities.

Supercapacitors are typically fabricated by introducing high surface-area materials (in order to induce electrochemical double-layer capacitance (EDLC)-based storage) or pseudocapacitive materials including conducting polymers and metal oxides (in order to induce charge transfer-based storage).<sup>6</sup> In general, pseudocapacitive materials provide higher energy

densities due to their ability to provide redox-based charge transfer.

Various metal oxides and conducting polymers have been used as pseudocapacitive materials, including RuO<sub>2</sub>, MnO<sub>2</sub>, NiO, Co<sub>2</sub>O<sub>3</sub>, polyaniline, and polypyrrole; however, these materials are often limited by their low conductivity and electrochemical stability when compared to carbon materials. Transition metal sulfides are relatively recent electrode materials that have shown promising pseudocapacitive performance in supercapacitors.<sup>8</sup> NiCo<sub>2</sub>S<sub>4</sub> is one such metal sulfide that has shown great promise in supercapacitors.<sup>9-11</sup> Binary metal sulfides like NiCo<sub>2</sub>S<sub>4</sub> (NCS) have been shown to provide higher electron conductivity than their oxide variants, and show further improvement over single component sulfides due to the increased capacity for redox reactions.<sup>12,13</sup> For example, Xiao *et al.* showed that the conversion of NiCo<sub>2</sub>O<sub>4</sub> to NCS nanotube arrays produced an increase in the areal capacitance from 0.52 F cm<sup>-2</sup> to 0.87 F cm<sup>-2</sup> at 4 mA cm<sup>-2</sup>.<sup>12</sup> Chen *et al.* found a similar phenomenon with NCS urchin-like nanostructures, achieving a gravimetric capacitance of 761 F g<sup>-1</sup> at 50 A g<sup>-1</sup>.<sup>13</sup> Yet, NiCo<sub>2</sub>S<sub>4</sub> still suffers from low structural stability and cyclability.<sup>14</sup>

These issues can be solved using the following strategies: (1) improving NCS structural stability using a conductive substrate such as graphene.<sup>15,16</sup> *In situ* growth of NiCo<sub>2</sub>S<sub>4</sub> on graphene can also increase the overall surface area of the metal sulfide and (2) improving NCS overall conductivity *via* doping, which can greatly improve electrode stability and capacitance.<sup>8,17-19</sup> To the

Chemical Engineering Department, University of Waterloo, 200 University Ave, Waterloo, Ontario, N2L 3G1, Canada. E-mail: zhwen@uwaterloo.ca

† Electronic supplementary information (ESI) available. See DOI: 10.1039/c7ta00897j

best of our knowledge, metal doping of NCS has yet to be accomplished in the literature but can be used to greatly improve its electrochemical properties.

Graphene-based materials are widely investigated for supercapacitor applications due to their superior electrical and mechanical characteristics and high surface areas. On the other hand, vanadium compounds have been widely used in supercapacitors due to their remarkable specific capacitance, superior conductivity, excellent long cyclability, and high ability of charge transfer reversibility which are all favorable for achieving high energy densities at high power densities in next-generation energy devices.<sup>15,20–22</sup>

Herein, we report for the first time a novel *in situ* vanadium modified NCS rooted on graphene sheets with superior electrochemical performance synthesized using a facile solvothermal process (Fig. 1A). Three types of material were synthesized and tested: pure NCS, graphene wrapped NCS (GNCS), and vanadium-doped graphene wrapped NCS (VNCS). The combination of excellent distribution of NCS on the graphene surface and vanadium modification (doping) leads to the formation of an ordered crystal structure of NCS nanosheets, highly improved performance at high power rates, and stability over long cycling periods with high capacitance retention. We also fabricated hybrid supercapacitors (HSCs) using the three materials to further investigate the improvements on electrochemical performance. The VNCS showed superior energy density at high power densities making it an excellent candidate for hybrid supercapacitor devices and opening the door for more investigation on this material.

## Results and discussion

### Characterization

Fig. 1B shows the XRD pattern of the NCS, GNCS and VNCS samples. All samples showed similar diffraction peaks around  $26.75^\circ$ ,  $31.50^\circ$ ,  $38.10^\circ$ ,  $50.35^\circ$ , and  $55.30^\circ$  corresponding to the (220), (311), (400), (511) and (440) planes of the cubic  $\text{NiCo}_2\text{S}_4$  phase (JCPDS card no. 43-1477) with no sign of impurities. No diffraction peaks can be observed for graphene which can be attributed to its low diffraction intensity.<sup>23</sup> The similarity of the three XRD patterns reveals that vanadium doping did not cause any noticeable changes to the crystal structure of the cubic NCS. To further investigate this, the peak corresponding to the (311) plane was magnified as shown in Fig. 1C, where a clear shift in the VNCS to a lower angle and higher intensity when compared to GNCS and PNCS samples can be seen. This can be attributed to the successful insertion of vanadium into the lattice of NCS.<sup>24,25</sup> This finding is in agreement with the TEM results discussed below which very clearly show that the dislocation in the (311) plane in VNCS resulted from vanadium insertion into the NCS lattice. Another shift is noticed in the (511) plane as seen in Fig. S1 (ESI<sup>†</sup>). The other planes showed almost identical peaks. The TGA analysis under air is shown in Fig. S1B (ESI<sup>†</sup>) and reveals that the vanadium-modified chalcogen is 85.3 wt% and rGO is 14.7 wt%.

The SEM images of NCS, GNCS and VNCS can be seen in Fig. 1D–F. Fig. 1D shows that the nanoparticles of NCS have the tendency to aggregate together forming larger size nanoparticles, while Fig. 1E shows how the graphene nanosheets wrap around the nanoparticles (an average size of 100 nm) and

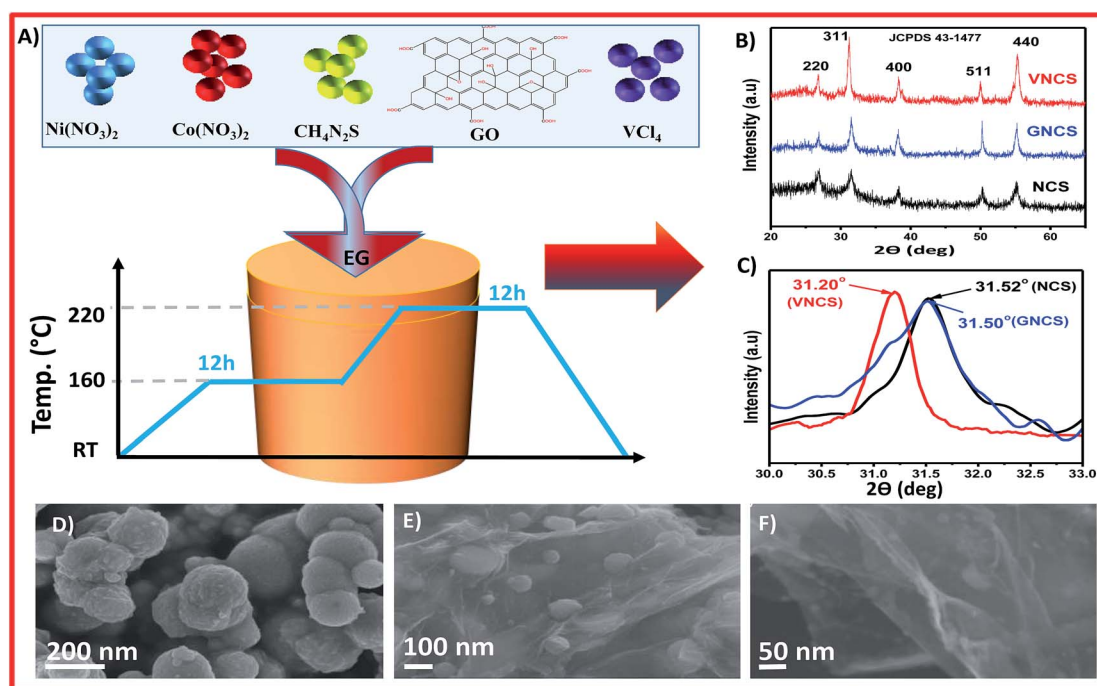


Fig. 1 (A) Experimental setup, (B) XRD pattern of all samples, (C) magnification of the XRD peak corresponding to the (311) plane of the three materials showing a negative peak for the VNCS, and (D–F) SEM images of NCS, GNCS and VNCS, respectively.

hinder particle agglomeration in the GNCS sample. The morphology in Fig. 1F reveals VNCS nanosheets are wrapped with, and laminated on, graphene nanosheets. This helps in hindering particle aggregation, enhancing electron transfer kinetics during charge–discharge operations due to graphene's high conductivity, and allowing for faster ion diffusion due to the increased contact area and uniform adhesion of VNCS on the graphene surface.<sup>23,26,27</sup> More SEM images showing graphene wrapping the NCS in GNCS can be seen in Fig. S2 (ESI<sup>†</sup>). For more investigation on the effect of V-doping on the chemical composition of the NCS, X-ray photoelectron spectroscopy (XPS) was used to analyze the elemental species and chemical composition changes (Fig. 2). Fig. 2A–E show the XPS spectra of the VNCS sample. The C 1s spectra shown in Fig. 2A reveal the peak at 284.62 eV due to the sp<sup>2</sup> carbon–carbon double bond of graphite (C=C). The peak at 286.1 eV is indexed to the carbon–oxygen double bond (C=O) and the weak peak at 288.2 eV is indexed to the carbon–oxygen single bond (C–O).<sup>14,28</sup> Fig. 2B shows the Ni 2p spectra, where the low energy band peak at 854.05 eV and the high energy band peak at 871.75 eV can be indexed to Ni<sup>2+</sup>, whereas the low and high energy band peaks at 856.1 and 873.78 eV, respectively are indexed to Ni<sup>3+</sup>. In the Co 2p spectra (Fig. 2C), the peaks at 779.45 and 795.6 are indexed to Co<sup>3+</sup>, whereas the peaks at 781.68 eV and 797.10 eV are indexed to Co<sup>2+</sup>. Fig. 2D shows the S 2p spectra where two peaks at 162.05 eV and 163.30 eV are found with one shake up satellite at 169.20 eV. The peak at 162.05 eV is indexed to the sulfur ions in low coordination on the surface and the peak located at 163.30 eV is indexed to the standard metal–sulfur bond.<sup>13,14,29</sup> The XPS spectrum of V 2p is shown in Fig. 2E with two distinguished main peaks at 516.40 eV and 524.10 eV. Both peaks are indexed to pentavalent vanadium.<sup>15,30–32</sup> The

XPS spectra of NCS and GNCS samples are shown in Fig. S3 (ESI<sup>†</sup>).

Fig. 2F–H show comparison of binding energies between NCS, GNCS, and VNCS for Ni 2p, Co 2p, and S 2p, respectively. The results show similar peaks for NCS and GNCS samples whereas VNCS shows shift in the binding energy of Ni 2p, Co 2p, and S 2p to lower values, suggesting a change in the electron cloud density around these elements due to the insertion of pentavalent vanadium.<sup>33–35</sup> The XPS atomic ratio analysis of the three samples shows the following stoichiometric ratios: Ni<sub>0.98</sub>Co<sub>1.99</sub>S<sub>4.03</sub>, NiCo<sub>2.01</sub>S<sub>3.99</sub>, and Ni<sub>0.98</sub>Co<sub>1.98</sub>V<sub>0.04</sub>S<sub>4.03</sub> for NCS, GNCS, and VNCS samples, respectively. These results suggest that the atomic ratios between Ni, Co, and S very closely match the stoichiometric formula (NiCo<sub>2</sub>S<sub>4</sub>) and that vanadium is successfully inserted into the lattice of NCS without substituting any element. This further explains the crystal dislocation shown in the TEM images and the plane shift shown in the XRD results. More information about the peaks including binding energies, FWHM and atomic ratios can be seen in Table S1 (ESI<sup>†</sup>).

Fig. 3 shows the TEM images of VNCS. The low magnification TEM image seen in Fig. 3A reveals the homogenous distribution of NCS nanosheets on the surface of the graphene nanosheets. Fig. 3B shows the TEM image of GNCS with graphene wrapping the NCS nanoparticles. Fig. 3C shows a higher magnification TEM image of the VNCS nanosheets laying on graphene sheets while Fig. 3D shows the selected area diffraction pattern (SAD) which reveals the polycrystalline structure of the VNCS with the different planes identified. Fig. 3E shows an HRTEM image of the (311) plane and the lattice dislocation. This finding is very clear evidence of the successful insertion of vanadium into the lattice of NCS which agrees with the XRD and XPS results and explains the reason for the improved electrochemical performance as discussed in the next section. Fig. 3F is obtained by high angle

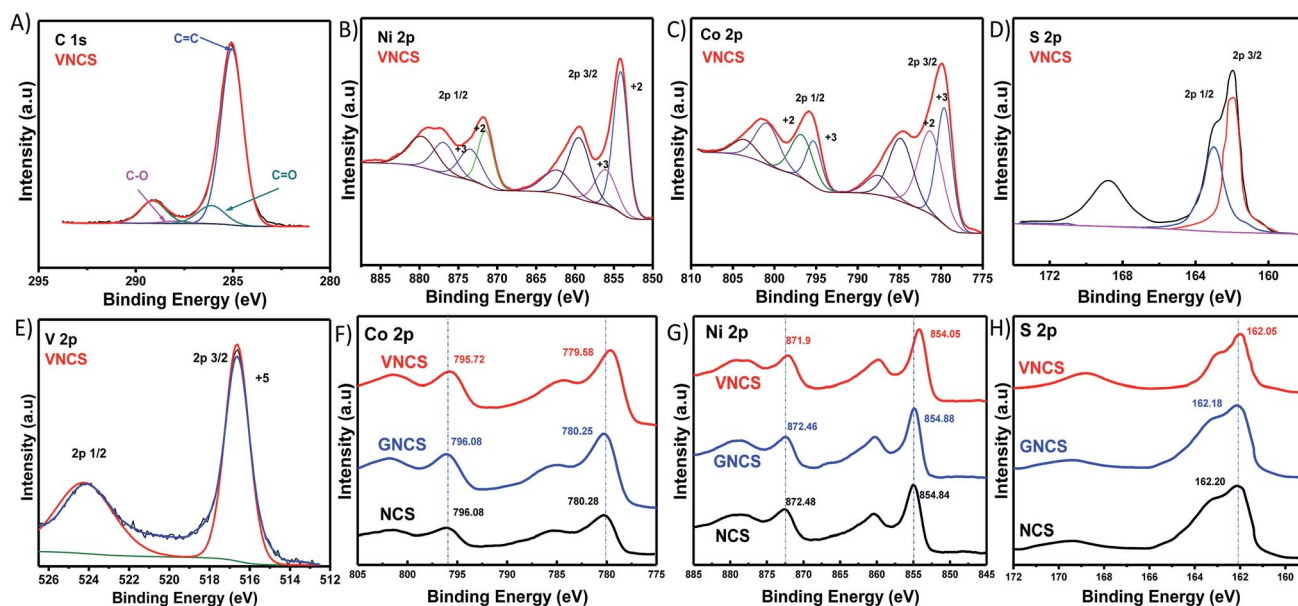
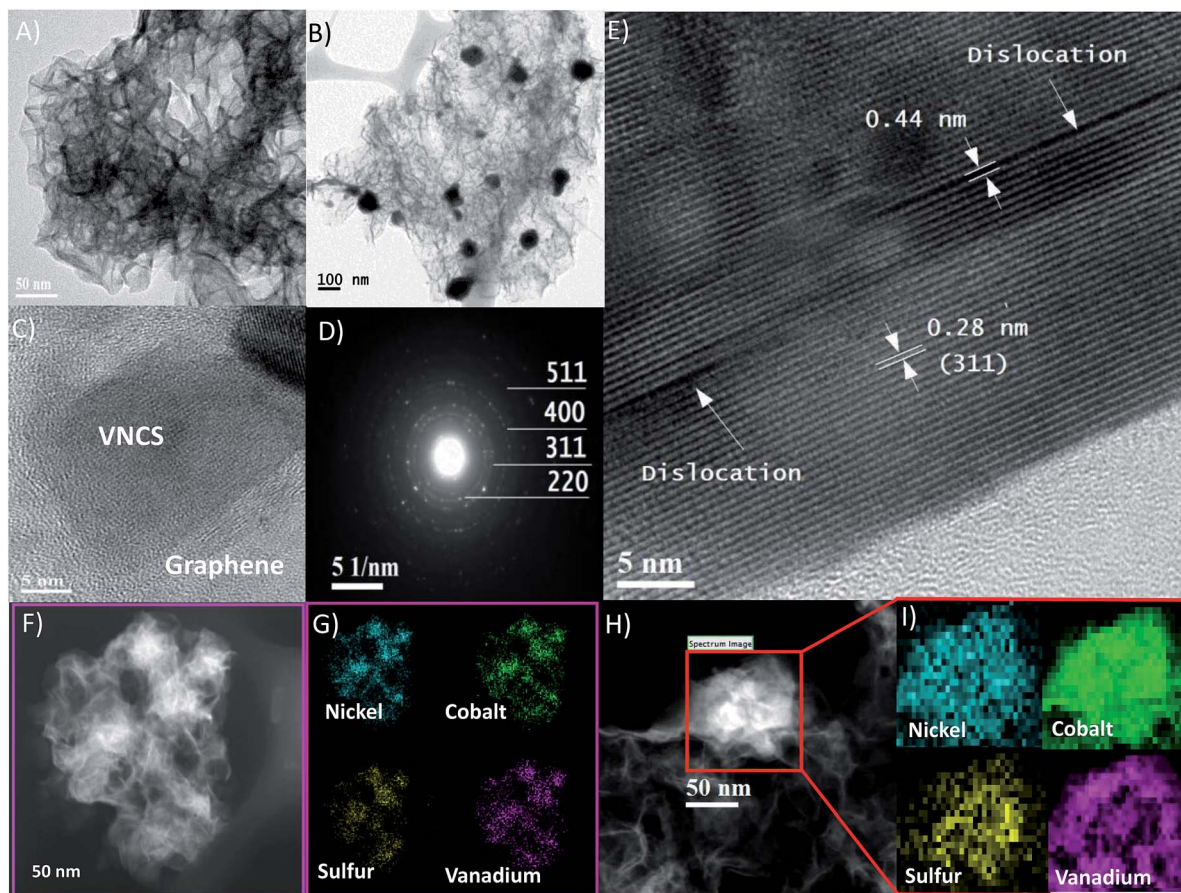


Fig. 2 XPS spectra measurements (A–E) XPS of VNCS showing C 1s, Ni 2p, Co 2p, S 2p and V 2p, respectively, and (F–H) XPS spectra comparison of all samples for Ni 2p, Co 2p, and S 2p, respectively, showing shift in the binding energy of the VNCS sample.



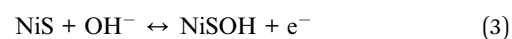
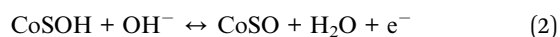
**Fig. 3** (A) TEM image of VNCS showing the sheet-on-sheet structure, (B) TEM image of GNCS showing graphene wrapped nanoparticles, (C) TEM image showing VNCS laying on the graphene surface, (D) SAD with the different planes identified, (E) HRTEM showing the dislocation in the crystal, (F) HAADF-STEM image showing the EDS investigation area, (G) EDS mapping of image (F) showing Ni, Co, S, and V, (H) EELS investigation area, and (I) EELS mapping of the selected area in image (H) showing the Ni, Co, S, and V with each pixel equivalent to  $3.6 \times 3.6$  nm.

dark-field scanning transmission electron microscopy (HAADF-STEM) and shows the selected area for elemental mapping. The elemental mapping is shown in Fig. 3G. The images reveal the homogenous distribution of all elements in the structure of VNCS that is also uniformly distributed onto the graphene surface, as shown in Fig. 3A and C. For deeper analysis of the atomic distribution within the VNCS structure, electron energy loss spectroscopy (EELS) was used. Fig. 3H shows the EELS investigation area, while Fig. 3I shows the EELS results of Ni, Co, S, and V elements. The results reveal the excellent distribution of all elements on the atomic level (one pixel in these images is equivalent to  $3.6 \times 3.6$  nm).

### Electrochemical performance

The electrochemical behavior of half-cell electrodes was analyzed in a three electrode setup using a platinum sheet ( $1.5 \text{ cm} \times 1.5 \text{ cm}$ ) as a counter electrode, a saturated calomel electrode (SCE) as the reference electrode, and the synthesized material as the working electrode. The tests were carried out in 2 M KOH electrolyte. The working electrodes were fabricated using the active material (80 wt%), super P carbon (10 wt%), and polyvinylidene-fluoride (10 wt%), with *N*-methyl-pyrrolidone (NMP) solvent to

prepare a slurry. The slurry was deposited on a pre-cleaned nickel foam ( $1.5 \times 1.5 \text{ cm}$ ) using a drop casting method before drying at  $60^\circ \text{C}$  for 2 hours in a convection oven and 12 hours in a vacuum oven at  $80^\circ \text{C}$ . The electrodes were then pressed under 10 MPa. The mass loadings of the three electrodes were 2.25, 2.03 and 2.18  $\text{mg cm}^{-2}$  for NCS, GNCS and VNCS, respectively. This range of mass loadings was selected to give the highest areal capacitance as can be seen in Fig. S4D (ESI<sup>†</sup>). The cyclic voltammetry (CV) of all samples at  $20 \text{ mV s}^{-1}$  and a voltage range of ( $-0.2 \text{ V}$  to  $+0.6 \text{ V}$ ) can be seen in Fig. 4A, while Fig. 4B shows the CV measurements of VNCS at various scan rates. All measurements show two peaks revealing the pseudo-capacitive characteristics resulting from the reversible faradic redox reactions of  $\text{Co}^{2+}/\text{Co}^{3+}$  and  $\text{Ni}^{2+}/\text{Ni}^{3+}$  as per the following equations:<sup>10,11</sup>



The results shown in Fig. 4A reveal that GNCS and VNCS have larger CV curve areas compared to the NCS sample,

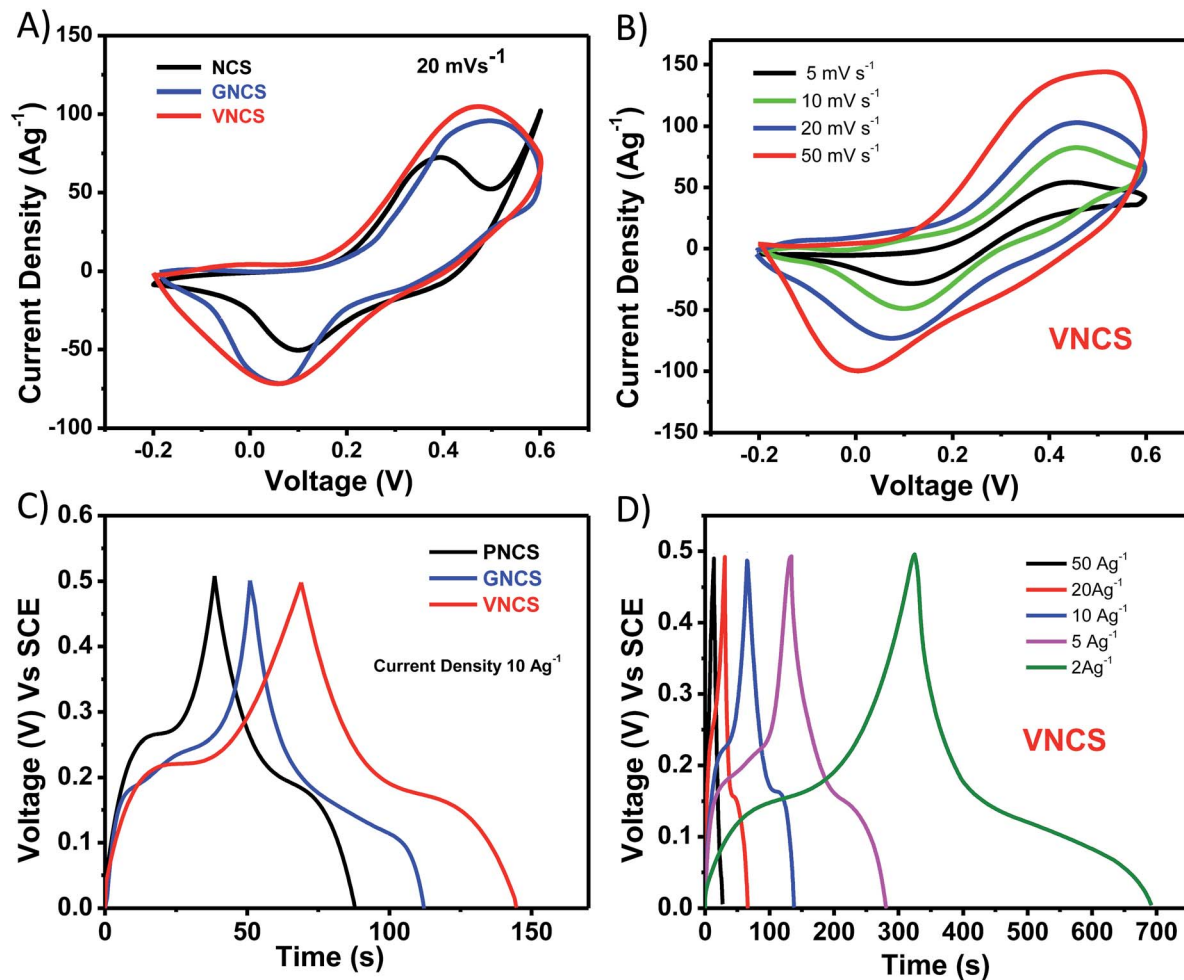


Fig. 4 Electrochemical measurements: (A) CV of the three samples at 20 mV s<sup>-1</sup>, (B) CV curves of VNCS at different scan rates, (C) galvanostatic charge–discharge of all samples at 10 A g<sup>-1</sup>, and (D) galvanostatic charge–discharge of VNCS at different current rates.

indicating higher specific capacitance in these samples which is attributed to the additional capacitance added by graphene and vanadium.<sup>21,36</sup> The CV test for the nickel foam alone can be seen in Fig. S4A,† indicating the negligible effect of the nickel foam and confirms that the pseudocapacitive characteristics in the CV measurement are mainly from the active material. Fig. S4B and C (ESI†) show the CV data of the CNS and GNCS samples at various scan rates. Fig. 4C shows the galvanostatic charge–discharge measurements of all materials at 10 A g<sup>-1</sup>, while Fig. 4D shows the charge–discharge measurements of the VNCS sample at multiple current rates. The results show symmetric charge–discharge processes for all samples and reveal stable pseudocapacitive performance of the synthesized materials.

Fig. 5A shows the specific capacitance of all samples at various current rates. The specific capacitance is obtained using the equation below:<sup>36</sup>

$$C_s = I/(m\Delta V/\Delta t) \quad (4)$$

where  $C_s$  is the specific capacitance (F g<sup>-1</sup>),  $I$  is the discharge current (A),  $m$  is the mass of the active material (g) and  $\Delta V/\Delta t$  is the discharge curve slope (V s<sup>-1</sup>) obtained after the voltage drop.

It can be seen from the curves that the GNCS shows higher initial capacitance and much better capacitance retention at higher power rates when compared to NCS. This improvement can be attributed to the effect of graphene in reducing particle aggregation, providing a larger surface area with more electroactive sites for ion diffusion, enhancing the charge/discharge kinetics, and allowing for faster electron transport.<sup>15,23,26,37</sup> It is also shown that both GNCS and VNCS show almost a similar initial capacitance at 2 A g<sup>-1</sup>. However, a distinction in performance arose as the current density increased. GNCS retains 75.7% of its capacitance from 2 to 20 A g<sup>-1</sup>; while, VNCS retains 90.2% of its capacitance from 2 to 20 A g<sup>-1</sup>. The distinguished performance of the VNCS continued as the current rate increased from 20 A g<sup>-1</sup> to 50 A g<sup>-1</sup> with only 6.5% capacitance loss compared to 9.1% for the GNCS. Moreover, the capacitance of the VNCS remained higher than 1000 F g<sup>-1</sup> (1024 F g<sup>-1</sup>) even at 50 A g<sup>-1</sup> compared to 810 F g<sup>-1</sup> and 237.76 F g<sup>-1</sup> for GNCS and NCS, respectively. These values represent 23.5%, 61%, and 76.4% capacitance retention compared to the capacitance of each sample at 2 A g<sup>-1</sup>. A comparison between the capacitance values of NCS and VNCS at low and high current densities can

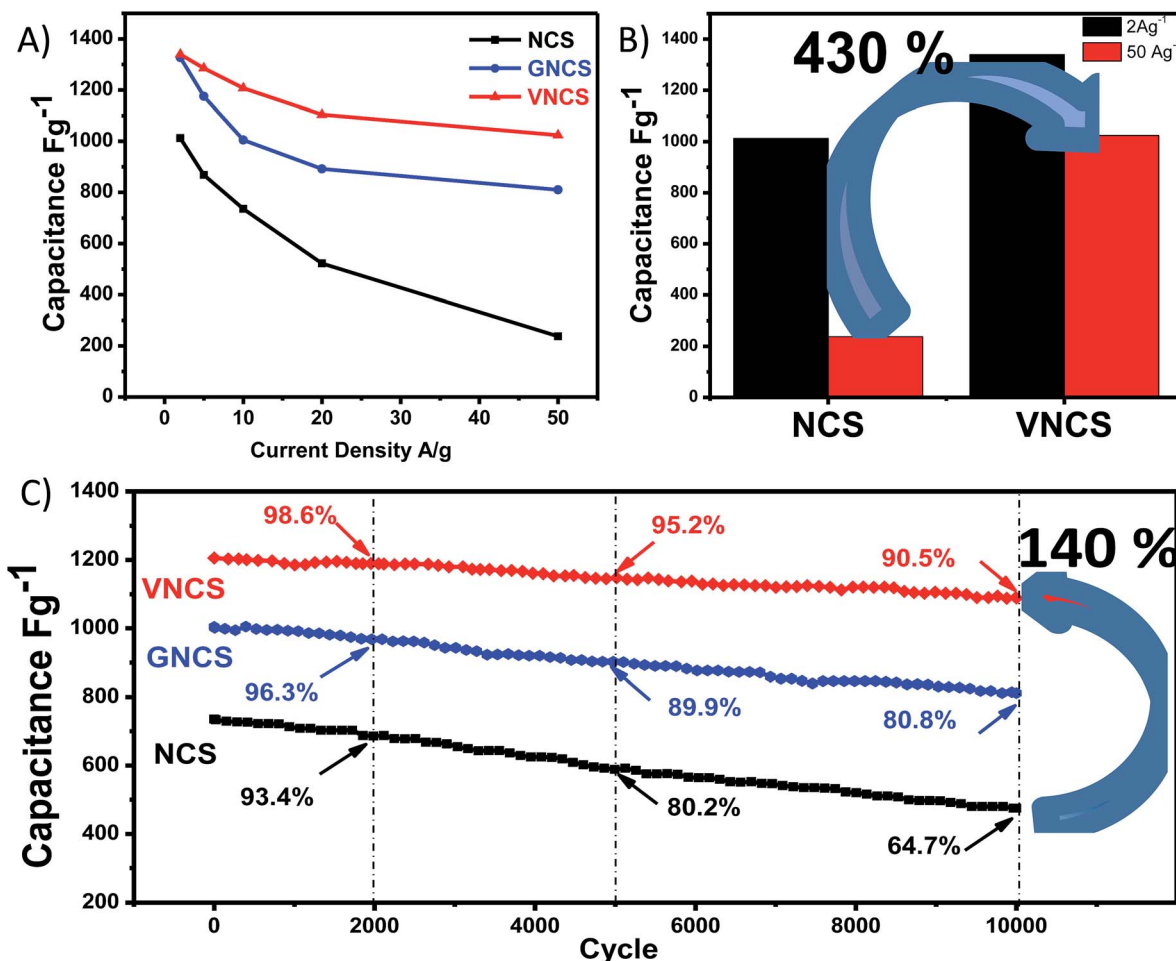


Fig. 5 (A) Specific capacitance of all samples at different current densities, (B) performance comparison between NCS and VNCS at low and high current densities and, (C) long cycling performance of the three samples for 10 000 cycles.

be seen in Fig. 5B. The results clearly reveal the outstanding improvement in capacitance at high current density for the VNCS sample with a 430% increase compared to the NCS sample. The charge–discharge data of NCS and GNCS at various current rates can be seen at Fig. S5 (ESI<sup>†</sup>). The summary of specific capacitance values of all materials at various current rates is shown in Fig. S6A (ESI<sup>†</sup>). The capacitance retention at various current rates compared to capacitance at  $2 \text{ A g}^{-1}$  is shown in Fig. S6B (ESI<sup>†</sup>). The results reveal that VNCS showed superior performance at all current rates compared to NCS and GNCS. The cycling stability of all samples was examined at  $10 \text{ A g}^{-1}$  (Fig. 5C). The capacitance retention values after 10 000 cycles are 64.7%, 80.8%, and 90.5% for NCS, GNCS, and VNCS, respectively. The VNCS showed around 140% higher capacitance retention than NCS and remarkably higher than the GNCS sample, losing only  $\sim 10^{-3} \text{ F}$  per cycle. All samples showed high coulombic efficiency throughout the cycling test as can be seen in Fig. S7 (ESI<sup>†</sup>) indicating high material stability. VNCS and GNCS showed higher coulombic efficiency compared to NCS which can be attributed to the graphene and vanadium doping effect, providing improved reversible charge and discharge kinetics.

The charge–discharge and long cycling results clearly demonstrate the impact of graphene and vanadium doping in enhancing the electrochemical performance of the device. We believe that the improved sheet-on-sheet interaction is behind the high stability and performance presented by VNCS, which results in the following: (1) allows for faster ion diffusion due to the increased number of electroactive sites which resulted from the increased contact area between the VNCS sheets and graphene sheets in addition to the uniform distribution of all elements of VNCS;<sup>23</sup> (2) generating a strong covalent interaction of the transition metal chalcogens onto the graphene surface, which explains the long cycling stability;<sup>38,39</sup> and, (3) improving the overall conductivity, pseudocapacitance, and stability through vanadium doping.<sup>21,25,36</sup> A comparison with recent reports is shown in Table S2 (ESI<sup>†</sup>); our work is the first report of its kind to report V-doped graphene wrapped NCS. The obtained performance is one of the best reported so far.

To further investigate the effect of graphene wrapping and V-doping on the electrochemical performance of NCS, we fabricated asymmetric hybrid supercapacitors (HSCs). The positive electrode in each one of these HSCs was made from one of the three synthesized materials, while the negative electrode for all

HSC devices was made from a composite of activated carbon and graphene (AC/G) in a mass ratio of 9 : 1. The AC/G material was also coated on nickel foam using a drop casting method. The mass ratio of the active material in the cathode to the active material in the anode was controlled to balance the charge on both electrodes ( $q^+ = q^-$ ) because of the difference in the charge storage mechanism in each electrode (faradic and EDLS) using the following well known charge balance equations:

$$q = C\Delta Vm \quad (5)$$

$$m^+/m^- = C^-\Delta V^-/(C^+\Delta V^+) \quad (6)$$

where  $q$  is the charge,  $m$  is the mass,  $C$  is the capacitance and  $\Delta V$  is the voltage window. The capacitance of AC/G is  $173 \text{ F g}^{-1}$  obtained from the charge–discharge test that can be seen in Fig. S8B (ESI<sup>†</sup>).

The electrochemical measurements were conducted using a similar electrolyte medium (2 M KOH) but in a higher voltage window (0–1.6 V). The voltage range was increased after the AC/G electrode showed excellent electrochemical reversibility in

a voltage window (–1.0 to 0) V for both CV and CD tests (Fig. S8 (ESI<sup>†</sup>)). The CV results of the three HSCs at  $20 \text{ mV s}^{-1}$  can be seen in Fig. 6A. All curves show hybrid capacitance from both EDLC and faradic redox reactions where the two redox peaks are still present. Fig. 6B shows the CV results of the VNCS-HSC device at various scan rates. It is noticed that the behavior of the curves do not change with increasing scan rates suggesting excellent reversible charge–discharge operations and stable hybridization between the two reaction mechanisms at the cathode and anode.<sup>11,40</sup> Fig. S9 (ESI<sup>†</sup>) shows the CV test of CNS-HSC and GNCS-HSC devices at various scan rates. The charge–discharge measurements of all HSCs at  $10 \text{ A g}^{-1}$  are shown in Fig. 6C, while Fig. 6D shows the charge–discharge measurements of the VNCS-HSC at various current rates. Both figures demonstrate that all devices have symmetric charge–discharge profiles at all current rates, revealing stable and well balanced reaction kinetics between the pseudocapacitive and EDLC parts of the HSC.

The calculated specific capacitance is shown in Fig. 7A using eqn (5) and (6) above using the total mass of the active material

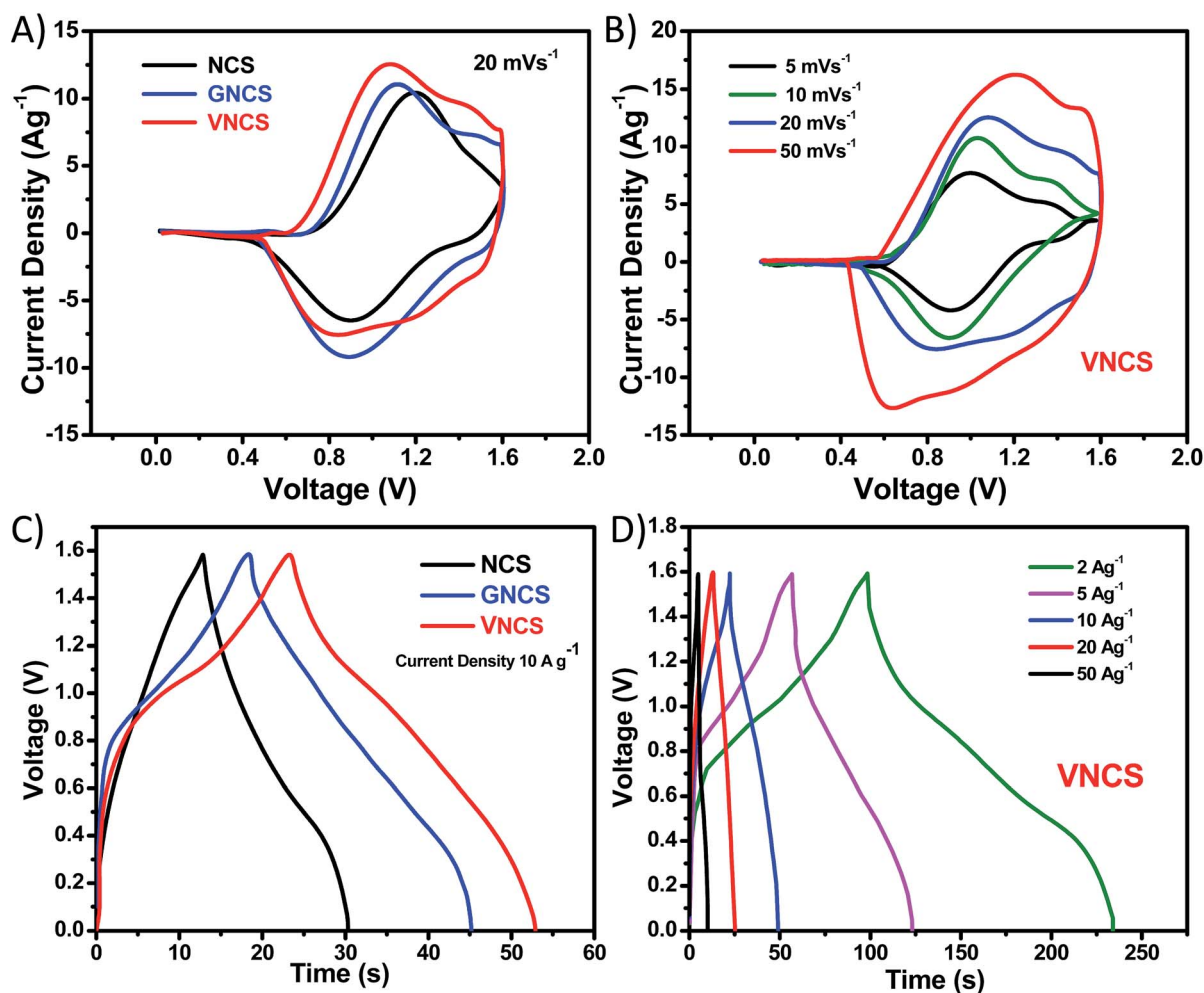


Fig. 6 Electrochemical measurements of HSC devices, (A) CV of all devices at  $20 \text{ mV s}^{-1}$ , (B) CV of the VNCS-HSC at different scan rates, (C) galvanostatic charge–discharge of all devices at  $10 \text{ A g}^{-1}$ , and (D) galvanostatic charge–discharge of the VNCS-HSC sample at different current densities.

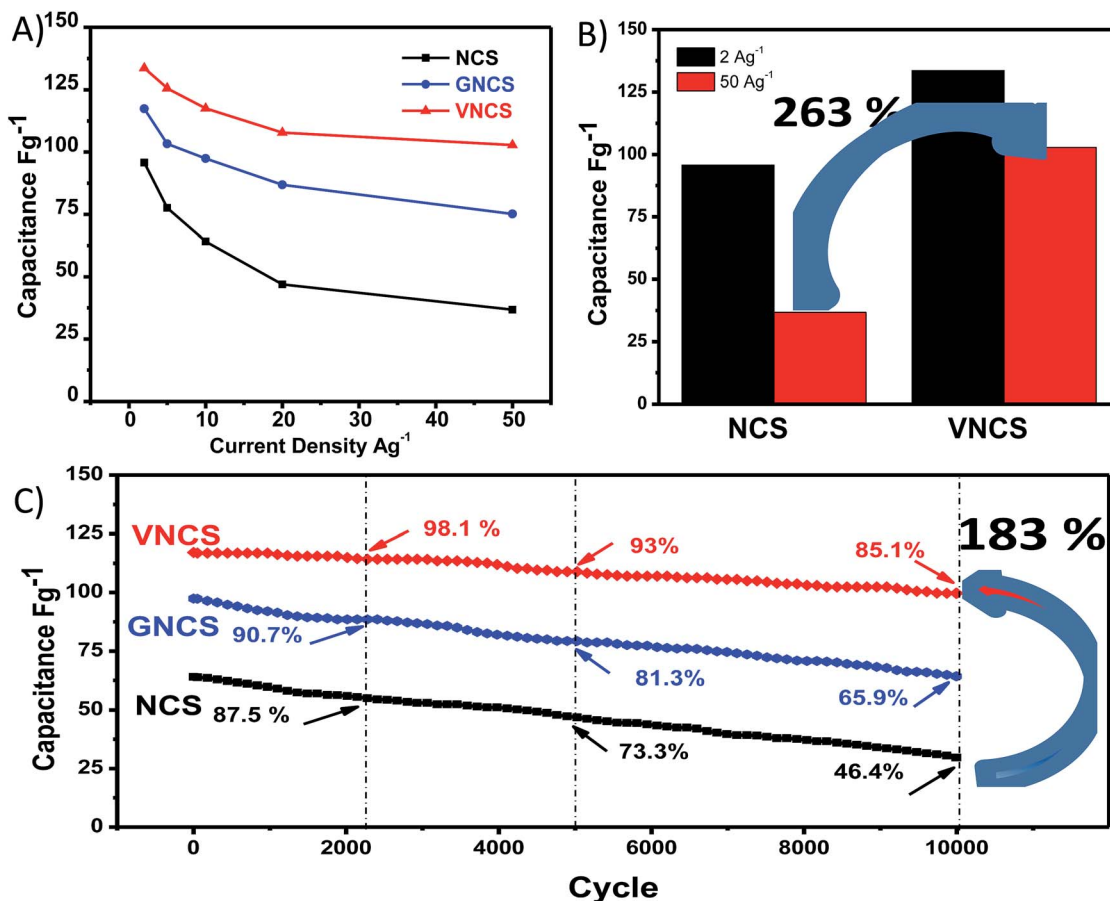


Fig. 7 (A) Specific capacitance of all HSC devices at different current densities, (B) performance comparison between NCS-HSC and VNCS-HSC devices at low and high current densities and, (C) long cycling performance of the three devices for 10 000 cycles.

in both the cathode and anode. The results show that the VNCS-HSC exhibited higher initial capacitance and remarkable capacitance retention at higher current densities compared to the other two devices. This significant improvement can be attributed to the crucial effect of vanadium's high specific capacitance and higher conductivity.<sup>15</sup> The results also show the effect of graphene wrapping in improving the initial capacitance and capacitance retention in the GNCS-HSC compared to the NCS-HSC. Fig. 7B shows a comparison between the capacitance of NCS-HSC and VNCS-HSC devices at 2 A g<sup>-1</sup> and 50 A g<sup>-1</sup>. It is noticed that the VNCS-HSC shows around 260% higher specific capacitance at a high current rate of 50 A g<sup>-1</sup> compared to the NCS-HSC, which further demonstrates the important effect of vanadium doping on electrochemical performance at high power rates.

The charge-discharge curves of the NCS-HSC and GNCS-HSC at various current rates are shown in Fig. S10A and B (ESI<sup>†</sup>). Fig. S11A (ESI<sup>†</sup>) shows the specific capacitance values of all HSC devices at various current rates, while Fig. S11B (ESI<sup>†</sup>) shows the capacitance retention of all HSC devices at different current densities compared to the capacitance of each device at a low current rate of 2 A g<sup>-1</sup>. All of these results further demonstrate the superior performance of the VNCS-HSC device at all current densities.

Fig. 7C shows the long-term cycling stability of all devices at 10 A g<sup>-1</sup>. The NCS-HSC shows 46.4% capacitance retention after 10 000 cycles while the GNCS-HSC shows 65.9% retention. The VNCS-HSC continued to show impressive improvements in electrochemical performance with 85.1% capacitance retention after 10 000 cycles which is not only higher than those of the NCS-HSC and GNCS-HSC, but also among the highest results reported in the literature.<sup>10,11,13,15,23,40-44</sup>

Fig. 8 shows the Ragone plot of all HSC devices. The calculations are based on the discharge curves using the following equations:

$$ED = 0.5C\Delta V^2 \quad (7)$$

$$PD = ED/d_t \quad (8)$$

where ED represents the energy density,  $C$  is the specific cell capacitance calculated according to eqn (4) using the total mass of both electrodes,  $\Delta V$  is the voltage window, PD is the power density, and  $d_t$  is the discharge time.

The energy densities of 33 W h kg<sup>-1</sup>, 41.7 W h kg<sup>-1</sup>, and 44.9 W h kg<sup>-1</sup> were obtained for NCS-HSC, GNCS-HSC, and VNCS-HSC devices, respectively, at an average power density of 0.87 kW kg<sup>-1</sup>. The VNCS-HSC still exhibits outstanding performance with an energy density of 33.6 W h kg<sup>-1</sup> at a high power density

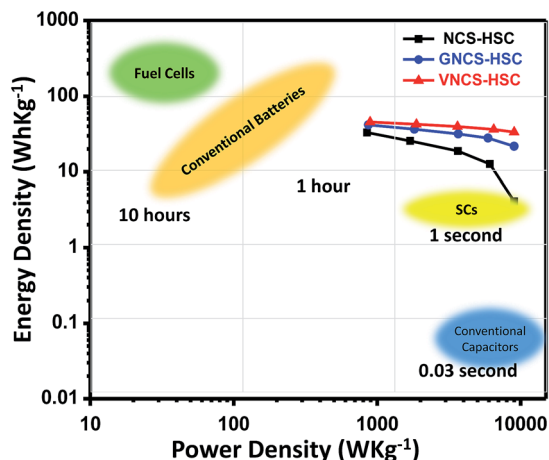


Fig. 8 Ragone plot showing the relationship between the power density and energy density of all HSC devices.

of  $9 \text{ kW kg}^{-1}$ . This remarkable result is 8 times higher than that of the NCS-HSC ( $4.2 \text{ W h kg}^{-1}$ ) and significantly higher than that of the GNCS-HSC ( $21/7 \text{ W h kg}^{-1}$ ). These results clearly demonstrate that the VNCS-HSC device can provide high power density while maintaining excellent energy density. This excellent performance makes VNCS a superior candidate for commercial applications of hybrid supercapacitors.

## Conclusion

In conclusion, vanadium-modified  $\text{NiCo}_2\text{S}_4$  nanosheets attached to the surface of graphene sheets were synthesized using a facile solvothermal method, resulting in a homogenous distribution of vanadium even at the atomic level. The V-doped sample showed outstanding electrochemical performance with a specific capacitance of  $1340 \text{ F g}^{-1}$  at a low current density of  $2 \text{ A g}^{-1}$  and  $1024 \text{ F g}^{-1}$  at  $50 \text{ A g}^{-1}$ . The vanadium-modification of  $\text{NiCo}_2\text{S}_4$  significantly improved the long cycling performance with less than  $10^{-3}$  F per cycle capacitance loss after 10 000 cycles. The material was also tested in a full cell hybrid supercapacitor and showed outstanding electrochemical performance and harmonized synchronization between the EDLC and faradic charge storage kinetics. The resulting hybrid supercapacitor showed improved electrochemical performance during charge–discharge operations, remarkable improvement in cycling stability and high energy density at high power densities, making it a superior material for hybrid supercapacitors and a potential candidate to bridge the energy/power gap between batteries and supercapacitors.

## Experimental section

### Materials

All materials were sourced from Sigma Aldrich and used as received.

### Synthesis of NCS

1 mmol of  $\text{Ni}(\text{NO}_3)_2 \cdot 6\text{H}_2\text{O}$  dissolved in 1 ml deionized distilled water (DDI) water and 2 mmol of  $\text{Co}(\text{NO}_3)_2 \cdot 6\text{H}_2\text{O}$  dissolved in 1

ml DDI were added to 4 mmol of thiourea (TU) dissolved in 2 ml DDI after being heated for few minutes on a hot plate at  $60 \text{ }^\circ\text{C}$ . The mixture was mixed by vortexing and then sonicated for 10 minutes before being added to 25 ml ethylene glycol (EG). This precursor solution was sonicated for 1 hour before being placed in a 50 ml Teflon-lined autoclave. The material was heated to  $160 \text{ }^\circ\text{C}$  for 12 hours followed by  $220 \text{ }^\circ\text{C}$  for 12 hours. The solution was then filtered and washed with ethanol and DDI several times. The collected material was dried at  $60 \text{ }^\circ\text{C}$  for 3 hours in a convection oven before drying under vacuum at  $80 \text{ }^\circ\text{C}$  for 12 hours. Finally, the material was calcined in a tube furnace at  $300 \text{ }^\circ\text{C}$  for 3 hours under an argon atmosphere to improve crystallinity.

### Synthesis of GNCS and VNCS

For the GNCS synthesis, 43.6 mg graphene oxide (GO) synthesized using a modified Hummers' method was added to the previously described precursor solution before sonicating for 1 h. The rest of the steps were similar to the above procedure. For VNCS, 43.6 mg GO and 0.2 mmol  $\text{VCl}_4$  were added to the precursor solution described in pure  $\text{NiCo}_2\text{S}_4$  before sonicating for 1 h. The rest of the steps did not change. The selection of the synthesis regime is based on the fact that TU is stable below  $120 \text{ }^\circ\text{C}$ . TU acts as a reducing and allocating agent. TU molecules have a high dipole moment which helps the precursor molecules self-assemble onto the GO nanosheets where they anchor to the oxygenated groups. Around  $190 \text{ }^\circ\text{C}$ , TU starts to decompose along with the precursor and the reduction of GO is accelerated. As a result, nickel, cobalt and vanadium combine with sulfur to form the active material on the surface of rGO.<sup>45–48</sup> The reaction medium and conditions help accelerate the reduction of GO.<sup>49–51</sup>

### Morphology and structure characterization

Sample microstructure and morphology were analyzed using an X-ray diffractometer (Rigaku Miniflex 600 X-ray Diffractometer) located at the Clean Energy and Applied Material Laboratory–University of Waterloo. TGA was performed using a TGA Q500 located at the analytical lab at the University of Waterloo. The X-ray photoelectron spectroscopy (XPS) analysis was done at the Ontario Center for Characterization of Advanced Materials using a PHI Quantera XPS spectrometer located at the Ontario Center for Characterization of Advanced Materials (University of Toronto). Scanning electron microscopy was conducted using a ZEISS ULTRA PLUS SEM located at Waterloo Advanced Technology Laboratory (University of Waterloo). Transmission electron microscopy was performed using a JEOL 2010F TEM/STEM field emission microscope located at the Canadian Center for Electron Microscopy (CCEM) located at McMaster University, Ontario-Canada.

## Acknowledgements

The authors wish to acknowledge the support provided by the Natural Sciences and Engineering Research Council of Canada (NSERC), the University of Waterloo and the Waterloo Institute for Nanotechnology.

## References

- J. M. Tarascon and M. Armand, *Nature*, 2001, **414**, 359–367.
- M. Armand and J. M. Tarascon, *Nature*, 2008, **451**, 652–657.
- L. Dong, C. Xu, Y. Li, Z.-H. Huang, F. Kang, Q.-H. Yang and X. Zhao, *J. Mater. Chem. A*, 2016, **4**, 4659–4685.
- G. Ren, G. Ma and N. Cong, *Renewable Sustainable Energy Rev.*, 2015, **41**, 225–236.
- P. Sharma and T. S. Bhatti, *Energy Convers. Manage.*, 2010, **51**, 2901–2912.
- G. Wang, L. Zhang and J. Zhang, *Chem. Soc. Rev.*, 2012, **41**, 797–828.
- A. González, E. Goikolea, J. A. Barrena and R. Mysyk, *Renewable Sustainable Energy Rev.*, 2016, **58**, 1189–1206.
- C.-H. Lai, M.-Y. Lu and L.-J. Chen, *J. Mater. Chem.*, 2012, **22**, 19–30.
- J.-C. Chen, C.-T. Hsu and C.-C. Hu, *J. Power Sources*, 2014, **253**, 205–213.
- X. Li, Q. Li, Y. Wu, M. Rui and H. Zeng, *ACS Appl. Mater. Interfaces*, 2015, **7**, 19316–19323.
- L. Shen, J. Wang, G. Xu, H. Li, H. Dou and X. Zhang, *Adv. Energy Mater.*, 2015, **5**, 1400977.
- J. Xiao, L. Wan, S. Yang, F. Xiao and S. Wang, *Nano Lett.*, 2014, **14**, 831–838.
- H. Chen, J. Jiang, L. Zhang, H. Wan, T. Qi and D. Xia, *Nanoscale*, 2013, **5**, 8879–8883.
- T. M. Masikhwa, F. Barzegar, J. K. Dangbegnon, A. Bello, M. J. Madito, D. Momodu and N. Manyala, *RSC Adv.*, 2016, **6**, 38990–39000.
- J. Yang, C. Yu, X. Fan, S. Liang, S. Li, H. Huang, Z. Ling, C. Hao and J. Qiu, *Energy Environ. Sci.*, 2016, **9**, 1299–1307.
- J. Shen, P. Dong, R. Baines, X. Xu, Z. Zhang, P. M. Ajayan and M. Ye, *Chem. Commun.*, 2016, **52**, 9251–9254.
- G. Karthikeyan and C. K. Das, *Macromol. Symp.*, 2012, **315**, 98–105.
- Y. Hu, H. Liu, Q. Ke and J. Wang, *J. Mater. Chem. A*, 2014, **2**, 11753–11758.
- G. Shao, Y. Yao, S. Zhang and P. He, *Rare Met.*, 2009, **28**, 132–136.
- Q. T. Qu, Y. Shi, L. L. Li, W. L. Guo, Y. P. Wu, H. P. Zhang, S. Y. Guan and R. Holze, *Electrochem. Commun.*, 2009, **11**, 1325–1328.
- N. Wang, Y. Zhang, T. Hu, Y. Zhao and C. Meng, *Curr. Appl. Phys.*, 2015, **15**, 493–498.
- W.-C. Fang, *J. Phys. Chem. C*, 2008, **112**, 11552–11555.
- S. Peng, L. Li, C. Li, H. Tan, R. Cai, H. Yu, S. Mhaisalkar, M. Srinivasan, S. Ramakrishna and Q. Yan, *Chem. Commun.*, 2013, **49**, 10178–10180.
- J. Popović, B. Gržeta, B. Rakvin, E. Tkalčec, M. Vrankić and S. Kurajica, *J. Alloys Compd.*, 2011, **509**, 8487–8492.
- M. S. Arif Sher Shah, K. Zhang, A. R. Park, K. S. Kim, N.-G. Park, J. H. Park and P. J. Yoo, *Nanoscale*, 2013, **5**, 5093–5101.
- M. F. El-Kady, Y. Shao and R. B. Kaner, *Nat. Rev. Mater.*, 2016, **1**, 16033.
- R. Raccichini, A. Varzi, S. Passerini and B. Scrosati, *Nat. Mater.*, 2015, **14**, 271–279.
- G. He, M. Qiao, W. Li, Y. Lu, T. Zhao, R. Zou, B. Li, J. A. Darr, J. Hu, M.-M. Titirici and I. P. Parkin, *Adv. Sci.*, 2016, 1600214, DOI: 10.1002/adv.201600214.
- Q. Liu, Z. Wu, Z. Ma, S. Dou, J. Wu, L. Tao, X. Wang, C. Ouyang, A. Shen and S. Wang, *Electrochim. Acta*, 2015, **177**, 298–303.
- V. S. Nair, S. Sreejith, P. Borah, S. Hartung, N. Bucher, Y. Zhao and S. Madhavi, *RSC Adv.*, 2014, **4**, 28601–28605.
- M. E. A. Warwick, A. J. Roberts, R. C. T. Slade and R. Binions, *J. Mater. Chem. A*, 2014, **2**, 6115–6120.
- H. T. T. Nguyen, D. Jung, C.-Y. Park and D. J. Kang, *Mater. Chem. Phys.*, 2015, **165**, 19–24.
- J. G. Tao, J. S. Pan, C. H. A. Huan, Z. Zhang, J. W. Chai and S. J. Wang, *Surf. Sci.*, 2008, **602**, 2769–2773.
- G. Sadanandam, K. Lalitha, V. D. Kumari, M. V. Shankar and M. Subrahmanyam, *Int. J. Hydrogen Energy*, 2013, **38**, 9655–9664.
- S. Oswald, *Appl. Surf. Sci.*, 2015, **351**, 492–503.
- L. Liu, M. Min, F. Liu, H. Yin, Y. Zhang and G. Qiu, *J. Power Sources*, 2015, **277**, 26–35.
- Q. Ke and J. Wang, *J. Materiomics*, 2016, **2**, 37–54.
- G. Z. Magda, J. Pető, G. Dobrik, C. Hwang, L. P. Biró and L. Tapasztó, *Sci. Rep.*, 2015, **5**, 14714.
- D. Peyrot and F. Silly, *ACS Nano*, 2016, **10**, 5490–5498.
- W. Chen, C. Xia and H. N. Alshareef, *ACS Nano*, 2014, **8**, 9531–9541.
- J. Pu, F. Cui, S. Chu, T. Wang, E. Sheng and Z. Wang, *ACS Sustainable Chem. Eng.*, 2014, **2**, 809–815.
- J. Pu, T. Wang, H. Wang, Y. Tong, C. Lu, W. Kong and Z. Wang, *ChemPlusChem*, 2014, **79**, 577–583.
- G. Li and C. Xu, *Carbon*, 2015, **90**, 44–52.
- L. Yu, L. Zhang, H. B. Wu and X. W. Lou, *Angew. Chem., Int. Ed.*, 2014, **53**, 3711–3714.
- D. C. Higgins, F. M. Hassan, M. H. Seo, J. Y. Choi, M. A. Hoque, D. U. Lee and Z. Chen, *J. Mater. Chem. A*, 2015, **3**, 6340–6350.
- Y. Liang, Y. Li, H. Wang and H. Dai, *J. Am. Chem. Soc.*, 2013, **135**, 2013–2036.
- Z. D. Wang, M. Yoshida and B. George, *Comput. Theor. Chem.*, 2013, **1017**, 91–98.
- J. Madarász and G. Pokol, *J. Therm. Anal. Calorim.*, 2007, **88**, 329–336.
- S. Pei and H.-M. Cheng, *Carbon*, 2012, **50**, 3210–3228.
- Y. Liu, Y. Li, Y. Yang, Y. Wen and M. Wang, *J. Nanosci. Nanotechnol.*, 2011, **11**, 10082–10086.
- S. Dubin, S. Gilje, K. Wang, V. C. Tung, K. Cha, A. S. Hall, J. Farrar, R. Varshneya, Y. Yang and R. B. Kaner, *ACS Nano*, 2010, **4**, 3845–3852.